Atmospheric Entry Profiles from the Mars Exploration Rovers Spirit and Opportunity

Paul Withers[a,b,*] and Michael D. Smith[c]

[a] Center for Space Physics, Boston University, 725 Commonwealth Avenue, Boston, MA 02215, USA.

[b] Visiting Research Fellow, Planetary and Space Sciences Research Institute, The Open University, Walton Hall, Milton Keynes, MK7 6AA, Great Britain.

[c] NASA Goddard Space Flight Center, Code 693, Greenbelt, MD 20771, USA.

[*] Corresponding author email address: withers@bu.edu

Number of pages: 42

Number of figures: 8

Number of tables: 3

Proposed Running Head:

Spirit and Opportunity Entry Profiles

Editorial Correspondence to:

Paul Withers

Center for Space Physics, Boston University,

725 Commonwealth Avenue, Boston, MA 02215, USA.

Email: withers@bu.edu

Phone: (617) 353 1531

Fax: (617) 353 6463

Received _____; accepted _____

ABSTRACT

Accelerometer measurements made by Spirit and Opportunity during their entries through the martian atmosphere are reported. Vertical profiles of atmospheric density, pressure, and temperature with sub-km vertical resolution were obtained using these data between 10 and 100 km. Spirit's temperature profile is $\sim$ 10 K warmer than Opportunity's between 20 km and 80 km. Unlike all other martian entry profiles, Spirit's temperature profile does not contain any large amplitude, long wavelength oscillations and is nearly isothermal below 30 km. Opportunity's temperature profile contains a strong inversion between 8 and 12 km. A moderate dust storm, which occurred on Mars shortly before these two atmospheric entries, may account for some of the differences between the two profiles. The poorly known angle of attack and unknown wind velocity may cause the temperature profiles to contain errors of tens of Kelvin at 10 km, but these errors would be an order of magnitude smaller above 30 km. On broad scales, the two profiles are consistent with Mars Global Surveyor Thermal Emission Spectrometer (TES) pressure/temperature profiles. Differences exist on smaller scales, particularly associated with the near-isothermal portion of Spirit's profile and the temperature inversion in Opportunity's profile.

1. Introduction

Data from the entry, descent, and landing (EDL) of the two Mars Exploration Rovers (MERs), Spirit and Opportunity, have been used to obtain two profiles of martian atmospheric density, pressure, and temperature from ∼100 km to <10 km altitude. The thermal structure of the martian atmosphere is sensitive to radiative forcing from suspended dust and to diabatic heating associated with atmospheric dynamics (Zurek et al., 1992; Leovy, 2001). It is also perturbed by a wide variety of waves and tides (Leovy and Zurek, 1979; Banfield et al., 2000; Withers et al., 2003a). These are the first vertical profiles of martian atmospheric structure measured during dusty conditions that have good vertical resolution and good vertical coverage. The atmospheric processes that can be observed in such profiles were discussed by Magalhães et al. (1999), who also compared the advantages and disadvantages of this measurement technique to those of other techniques.

The MER project sent two nearly-identical rovers to Mars (Garvin et al., 2003; Squyres et al., 2004a,b). The "MER–2" rover, which was launched on the "MER–A" mission to Gusev Crater on 10 June 2003, was later renamed "Spirit". The "MER–1" rover, which was launched on the "MER–B" mission to Meridiani Planum on 7 July 2003, was later renamed "Opportunity". The positions, times, and dates of the two landings are shown in Table 1. Both spacecraft landed at early afternoon local solar times (LSTs). The design of the MER spacecraft for cruise and EDL was based on the successful Mars Pathfinder design (Spencer et al., 1999; Crisp et al., 2003). Each MER carried two Litton LN-200S inertial measurement units (IMUs), one mounted on the backshell and one mounted on the rover, which contained three identical silicon single-axis accelerometers and three identical fibre optic single-axis gyroscopes (Crisp et al., 2003; Kass et al., 2004). The MER project released to the Planetary Data System (PDS) data from the EDL phase of both MER missions (Kass et al., 2004). Kass et al. (2004) also describe the major events that occurred

during entry, the onboard data processing, and other ancilliary informations. This work used measurements of the acceleration at the spacecraft centre of mass, specifically 4 Hz backshell IMU measurements from the TRANSFORMED directory of the PDS archive.

[Table 1]

The structure of this paper is: the entry states of Spirit and Opportunity; the reconstruction of their trajectories; the reconstruction of atmospheric density, pressure, and temperature along those trajectories; the sensitivity of the results to the assumptions and approximations; and the scientific implications of the two density, pressure, and temperature profiles.

2. Entry States

An entry state, specifically a 3-component position vector, 3-component velocity vector, and a scalar for time, is required to reconstruct an entry trajectory from measured accelerations (Magalhães et al., 1999; Withers et al., 2003b). Some of the seven values that constitute the entry states of Spirit and Opportunity have not been published, so they are inferred in this section using other constraints.

Entry is defined to occur when the spacecraft's radial distance from the centre of mass of Mars reaches 3522.2 km (Kass et al., 2004). The radial distances to the landing sites are known (Table 1). Latitudes and longitudes at landing, but not entry, have been published (Table 1). The inertial velocities at entry were 5.63 km s^{-1} (Spirit) and 5.70 km s^{-1} (Opportunity) (Desai and Knocke, 2004). The inertial flight path angle at entry was 11.5° (Desai and Knocke, 2004). The time intervals between entry, which is not observable in the time series of measured accelerations, and parachute deployment, which is, are 251.0 s (Spirit) and 250.3 s (Opportunity) (Desai and Knocke, 2004). This list includes seven firm

constraints (radius at entry, speed at entry, flight path angle at entry, radius at landing, latitude at landing, longitude at landing, and time at entry). Four of these constraints directly specify four of the seven values that make up the entry state. The three remaining constraints are the landed radius, latitude, longitude and the three unknown values in the entry state are the entry flight path azimuth, latitude, and longitude.

A process of trial-and-error was used to determine the entry flight path azimuth, latitude, and longitude. First, values for the entry flight path azimuth, latitude, and longitude were assumed, which gave a complete entry state. Second, an entry trajectory was reconstructed, as described in Section 3, using this assumed entry state. Third, the landed radius, latitude, longitude were compared to their known values. This process led to the estimated entry states shown in Table 2. The sensitivity of the landed position to the entry flight path azimuth, latitude, and longitude can be illustrated as follows. Spirit's actual landed position was -14.6°N, 175.5°E, and a radius of 3392.3 km. Spirit's landed position using the estimated entry state is -14.5°N, 175.5°E, and a radius of 3392.4 km. If the flight path azimuth in the entry state is decreased by 1 degree, then Spirit's landed position becomes -14.3°N, 175.5°E, and a radius of 3392.4 km. If the latitude of the entry state is decreased by 1 degree, then Spirit's landed position becomes -15.5°N, 175.6°E, and a radius of 3392.4 km. If the longitude of the entry state is decreased by 1 degree, then Spirit's landed position becomes -14.5°N, 174.5°E, and a radius of 3392.4 km. Results for Opportunity are similar.

[Table 2]

3. Trajectory Reconstruction

The process of reconstructing a spacecraft trajectory using accelerometer data has been described previously, so it is only summarized here (Magalhães et al., 1999; Withers et al., 2003b). In the generic case, the total acceleration acting on the spacecraft is determined from the accelerometer data and a model of the martian gravitational field. These accelerations are then integrated forward in time using the equations of motion and an entry state. Time series of the position and velocity of the spacecraft are obtained by this process.

In practice, the most complicated part of this process is converting accelerations measured in a spacecraft-fixed frame into accelerations in a planet-fixed frame. It is clearly impossible to proceed if it is not known whether the measured accelerations are parallel or anti-parallel to the local vertical. Withers et al. (2003b) discussed several possible methods for performing this conversion. In principle, quaternions, which describe the relationship between a spacecraft-fixed frame and a planet-fixed frame, that are given in the PDS archive can be used to convert the measured accelerations into a planet-fixed frame (Kass et al., 2004). In practice, these quaternions appear to contain serious inconsistencies. If quaternions were included in the trajectory reconstruction in Section 2, then no combination of entry flight path angle, latitude, and longitude could be found that led to impact at the known landing site for Opportunity. The archived quaternions were derived from gyroscope measurements of angular rates and an initial condition for spacecraft orientation. It is possible that the initial condition used for Opportunity is inaccurate (personal communication, Kass, 2005).

Accelerations measured in a spacecraft-fixed frame were instead converted into accelerations in a planet-fixed frame using the "head-on" method of Withers et al. (2003b). This method assumes that the axial acceleration, a_z, was directed parallel to $\underline{v_{rel}}$ and

that the atmosphere rotated at the same fixed angular rate, $\underline{\Omega}$, as the solid body of Mars where Ω corresponds to a martian sidereal day of 24.6229 hours (Lodders and Fegley, 1998). The effects of neglecting winds will be discussed in Section 5. Axes x, y, z refer to a spacecraft-fixed frame, the z axis is parallel to the spacecraft's symmetry axis, $\underline{a}$ is aerodynamic acceleration, and $\underline{v_{rel}}$ is the velocity of the spacecraft relative to the atmosphere. The acceleration due to martian gravity is a known function of position:

$$\underline{g} = \nabla U \tag{1}$$

$$U = \frac{GM}{r} \left(1 + \left(\frac{R_{ref}}{r} \right)^2 C_{20} P_{20} \left(\cos \theta \right) \right) \tag{2}$$

$$P_{20} \left(x \right) = \sqrt{5} \, \frac{1}{2} \left(3x^2 - 1 \right) \tag{3}$$

where $\underline{g}$ is the acceleration due to the gravitational field of Mars in an inertial frame, U is the gravitational potential, GM is the product of the gravitational constant and the mass of Mars, R_{ref} is a reference radius, $r = |\underline{r}|$, $\underline{r}$ is position with respect to the centre of mass of Mars, P_{20} is the normalised associated Legendre function of degree 2 and order 0, θ is colatitude, and C_{20}, which is related to the oblateness of Mars, is the tesseral normalised spherical harmonic coefficient of degree 2 and order 0 (Tyler et al., 1992; Smith et al., 1993; Tyler et al., 2000). The sign and normalization conventions for U and P_{20} are defined by Equations 1–3. $C_{20} = -8.75981 \times 10^{-4}$, $GM = 4.2828 \times 10^{14}$ m^3 s^{-2}, and $R_{ref} = 3394.2$ km (Tyler et al., 2000). The use of higher order models of the gravitational field does not significantly alter the reconstructed trajectory or atmospheric structure (Magalhães et al., 1999). Note that this expression for $\underline{g}$ does not contain any centrifugal terms. Areocentric latitudes and longitudes were used throughout this paper.

Now that both aerodynamic and gravitational accelerations have been expressed in a planet-fixed frame, they can be summed to find the total acceleration acting on the

spacecraft and this acceleration can be used in the equations of motion. The trajectory reconstruction was performed using the procedures described in Withers et al. (2003b) and the reconstructed conditions at parachute deployment are shown in Table 3. Altitude is defined as $r - r_0$, where r is radial distance from the centre of mass of Mars and r_0 is the radial distance to the relevant landing site (Table 1). Note that both Spirit and Opportunity travelled 800 km horizontally between entry and parachute deployment.

[Table 3]

A Monte Carlo error analysis, based on normally distributed uncertainties, was used to quantify the uncertainties in the derived trajectories. Based on analysis of pre-entry data, the uncertainty in a_z was fixed at 0.01 m s^{-2}. Uncertainties in the entry states of Spirit and Opportunity were assumed to be the same as for Pathfinder (Table 2) (Magalhães et al., 1999). This is addressed further in Section 5. The uncertainties in the derived trajectories will be used to determine the uncertainties in the atmospheric structure in Section 4.

4. Atmospheric Structure Reconstruction

Atmospheric density, ρ, is related to a_z (Magalhães et al., 1999):

$$ma_z = \frac{\rho A v_{rel}^2 C_A}{2} \tag{4}$$

where m is the spacecraft mass, A is the reference area of the spacecraft, and C_A is the axial force coefficient, which is usually on the order of 2 (Withers et al., 2003b). Both spacecraft have A corresponding to a disc of diameter 2.648 m (Schoenenberger et al., 2005). Spirit's mass was 827.0 kg and Opportunity's mass was 832.2 kg (Desai and Knocke, 2004). Atmospheric pressure, p, is related to ρ by the equation of hydrostatic equilibrium:

$$\frac{dp}{dr} = \rho \times (g_r + c_r) \tag{5}$$

where g_r, which is negative and a function of position, is the radial component of Equation 1, and c_r is the radial component of $-\underline{\Omega} \times (\underline{\Omega} \times \underline{r})$. This centrifugal term is small and $|c_r/g_r| \sim 4 \times 10^{-3}$. Atmospheric temperature, T, is related to ρ and p by the ideal gas law:

$$\mu p = \rho \frac{R}{N_A} T \tag{6}$$

where $\mu = 43.49$ g mol^{-1} is the mass of one mole of the martian atmosphere, R is the universal gas constant, and N_A is Avogrado's number (Magalhães et al., 1999).

Equation 4 can be used to determine ρ from the results of Section 3. Other than ρ, the only unknown in Equation 4 is C_A. An aerodynamic database for the MER spacecraft has been published (Schoenenberger et al., 2005). It lists C_A, C_N, where C_N is the normal force coefficient, and the ratio a_n/a_z, where $a_n = \sqrt{a_x^2 + a_y^2}$, as single-valued functions of α for various speeds, atmospheric densities, and temperatures, where α, the angle of attack, is the angle between the spacecraft symmetry axis and $\underline{v_{rel}}$. This aerodynamic database was generated numerically using direct simulation Monte Carlo methods at high altitudes, where the flow is in the free molecular or transitional regimes, and computational fluid dynamics methods at low altitudes, where the flow is in the continuum regime. Wind tunnels and other physical testing techniques were not used. Withers et al. (2003b) have described how ρ, C_A, and α can be determined self-consistently using an iterative procedure and a_n/a_z. Since a_n is small compared to the measurement uncertainties at high altitudes, its value was fixed at 0 above about 80 km. The effects of this assumption are addressed in Section 5.

Either pressure or temperature must be specified at the top of the atmosphere to provide an upper boundary condition for Equation 5 and the accepted approximation that $p_0 = \rho_0 g_0 H_{\rho,0}$, where H_ρ is the measured density scale height and the subscript "0" refers to values at the top of the atmosphere, was used (Seiff et al., 1973; Seiff and Kirk,

1977; Seiff et al., 1980, 1998; Magalhães et al., 1999). This is equivalent to assuming that $T_0 = \mu_0 g_0 H_{\rho,0} N_A / R$. Since pressure varies exponentially with altitude, the effects of errors in p_0 or T_0 on the pressure and temperature profiles are small at low altitudes. An error of 50% in p_0 or T_0 corresponds to an error of less than 7% in p or T two scale heights below the top of the atmosphere and an error of less than 1% in p or T four scale heights below the top of the atmosphere (Withers et al., 2003b).

The Spirit and Opportunity profiles, which are shown in Figures 1–2, were measured in equatorial regions, at early afternoon LSTs, in late northern winter. Spirit's temperature profile does not contain any large amplitude, long wavelength oscillations. Spirit's temperature profile is a relatively smooth quadratic function of altitude above 30 km, but temperatures are almost isothermal below 30 km. Opportunity's temperature profile, which is ~ 20 K colder at 80 km than Spirit's is, has a large amplitude, long wavelength oscillation around 60 km. The temperature decreases by 15 K from 12 km to 8 km. These results will be discussed further in Section 6.

[Figures 1–2]

A Monte Carlo error analysis was used to quantify the uncertainties in the derived atmospheric structures. Uncertainties in the reconstructed position and velocity, obtained from Section 3, in C_A, and in the upper boundary condition for Equation 5 were included. Uncertainties in C_A were taken to be 5% and the uncertainty in T_0 was assumed to be 50 K (Magalhães et al., 1999; Desai et al., 2003; Schoenenberger et al., 2005). Sources of uncertainty in C_A include differences between the conditions used to calculate the aerodynamic database and those experienced during entry, as well as approximations in the numerical model. The altitude of the upper boundary was around 100 km. The effects of these uncertainties are shown in Figures 1–2.

5.   Sensitivity Studies

A number of approximations and assumptions were made in Sections 3–4. The flight path angle, latitude, and longitude at entry were determined indirectly using the radius, latitude, and longitude at landing. The axial acceleration, a_z, was assumed to be parallel to v_{rel}, giving an angle of attack of zero, for the trajectory reconstruction. Atmospheric winds were assumed to be zero for the trajectory and atmospheric structure reconstruction. The aerodynamic database that was used to find the axial force coefficient, C_A, and angle of attack for the atmospheric structure reconstruction was obtained from numerical simulations; it may contain errors. The angle of attack for the atmospheric structure reconstruction was found using the observed a_n, which is small compared to the measurement uncertainties at high altitudes. The pressure/temperature at the top of the atmosphere was estimated in order to provide an upper boundary condition for the equation of hydrostatic equilibrium. Pathfinder-like uncertainties in the entry state, uncertainties in the aerodynamic database, and uncertainties in the upper boundary condition were considered in Sections 3–4. In this section, the sensitivity of the results to the assumptions concerning the angle of attack, the wind speed, and the flight path angle, latitude, and longitude at entry are investigated. The sensitivity of the inferred trajectory and atmospheric structure to these assumptions increases with time since entry, so results are most sensitive at low altitudes.

The angle of attack, α, was assumed to be zero in Section 3, whereas its non-zero value in Section 4 was determined from the measured ratio a_z/a_n. The present structure of the software used in this work does not permit the angle of attack to be passed back and forth between the trajectory and atmospheric structure Monte Carlo error analyses. If the angle of attack is fixed at $0°$ or at $2°$ in Sections 3 and 4, then changes in the inferred trajectory and atmospheric structure are generally small. The changes in density and temperature

at parachute deployment are <2% and <3K. However, if the angle of attack is fixed at 5°, then the density and temperature at 30 km change by <1% and <3K, whereas the density, temperature, altitude, and atmosphere-relative speed at parachute deployment change by 7%, ∼20 K, 0.2 km, and 20 m s^{-1}. These changes are similar for both Spirit and Opportunity.

Wind speeds were assumed to be zero in Sections 3–4. Since neither the mean nor the standard deviation of the zonal and meridional wind speeds for the entries of Spirit and Opportunity were known as functions of altitude, non-zero wind speeds were not considered in the trajectory and atmospheric structure Monte Carlo error analysis. If the zonal wind is fixed at +30 m s^{-1} eastward throughout the atmosphere, then the density and temperature at 30 km change by +2% and -2K (Rafkin and Michaels, 2003; Toigo and Richardson, 2003). The density, temperature, altitude, and atmosphere-relative speed at parachute deployment change by +15%, -20K, +0.4 km, and -30 m s^{-1}. If the wind direction is reversed, then the sign of these changes is also reversed. These changes are similar for both Spirit and Opportunity.

Three parts of the entry state were determined indirectly in Section 2: flight path azimuth, latitude, and longitude. Changes in latitude and longitude at entry by ≈ 1° merely translate the entire trajectory horizontally, with negligible change in the inferred atmospheric structure. Changes in the flight path angle at entry by ∼ 5° change the latitude at 30 km and parachute deployment by ∼ 1°; changes in longitude are much smaller. Changes in the inferred atmospheric structure at 30 km are negligible, but changes in density and temperature at parachute deployment are 2% and 3K. These changes are similar for both Spirit and Opportunity.

The atmospheric profiles obtained in this work are therefore sensitive to assumptions concerning the angle of attack and wind speed. Likely errors in the entry state are less

important. The effects on atmospheric properties are small, on the order of 2%, above 30 km, but increase to the order of 10% at parachute deployment. Figures 3–4 show the temperature profiles obtained in some of these sensitivity studies, including the combined effect of fixing the angle of attack at 5° and the zonal wind speed at 30 m s^{-1}. The temperature range of the profiles in Figures 3–4 is 40K at 10 km, 15K at 20 km, and 5K at 30 km.

[Figure 3] [Figure 4]

Uncertainties in the angle of attack and wind speed have significant effects on the lowest parts of the reconstructed entry profiles. The profiles would be more scientifically useful if these uncertainties were smaller. Uncertainties in the angle of attack may be reduced in the future if the archived quaternions are corrected, which would permit direct determination of spacecraft orientation in a Mars-fixed frame and a more accurate trajectory reconstruction. The atmospheric structure reconstruction depends on the atmosphere-relative velocity of the spacecraft, which depends on the unknown wind velocity. It may be possible to estimate the wind velocity at low altitudes by comparing observed and predicted accelerations and angular rates, but this will be a challenging task.

The importance of the angle of attack can be understood through the following example. The acceleration parallel to $\underline{v_{rel}}$, $a_{\parallel}$, is $a_z \cos \alpha$. The measured quantity is a_z, but the physically important quantity is $a_{\parallel}$. Suppose an entry vehicle has $\alpha = 0$ ($\cos \alpha = 1$) above 60 km, $\alpha = 5°$ ($\cos \alpha = 1 - 0.004$, an apparently small change of 0.4%) between 60 km and 10 km, a speed of 5000 m s^{-1} at 60 km, and a speed of 500 m s^{-1} at 10 km. Using the technique of Section 3, $a_{\parallel}$ would be assumed to be identical to a_z, and the reconstructed change in velocity would be 4500 m s^{-1} / $(1 - 0.004)$ or 4518 m s^{-1}. The reconstructed speed at 10 km would be 482 m s^{-1}, not 500 m s^{-1}, a decrease of 3.6%. The reconstructed density at 10 km would be too large by 7.2%, and pressures and temperatures would also

be affected.

6.   Discussion of Results

6.1.   Effects of Dust

The dust loading in the martian atmosphere can increase significantly from its background level within a few days during the onset of a regional/global dust storm. Micron-sized dust particles, which can be lifted by 10–20 km by a dust storm, take days to fall one kilometre and the decay time of a large dust storm is on the order of months (Pollack et al., 1979; Murphy et al., 1990; Smith, 2004). The atmosphere can become hotter by $\sim$ 15 K over a broad vertical range during a large dust storm (Smith et al., 2001). Atmospheric dynamics are modified and some atmospheric tidal modes, especially the semidiurnal migrating tide, become stronger (Zurek et al., 1992; Bridger and Murphy, 1998). The effects of dust storms extend at least as high as 160 km (Keating et al., 1998). The effects on the atmosphere may have a global extent even if the region of high dust opacity is relatively small. A large regional dust storm began on Mars in December 2003 and raised significant amounts of dust near the Opportunity landing site.

Figure 5 shows infrared dust opacities, τ, measured near the landing sites of both Spirit and Opportunity by the nadir-looking Mars Global Surveyor (MGS) Thermal Emission Spectrometer (TES) instrument in December 2003 and January 2004. The values have been corrected for topographic differences between the two sites. The LSTs of all measurements was $\sim$13.5 hrs. The longitudes of the Spirit measurements are between 170 and 200°E; the longitudes of the Opportunity measurements are between -10 and 20°E. The latitudes of each series of measurements are within a few degrees of the latitudes of the respective landing sites. These zonal and meridional ranges are due to MGS's near-polar orbit, which

has a period ~ 2 hours. The 12 ground tracks that cross the equatorial region each day therefore have a zonal spacing of about $30°$. Some of the variability shown in Figure 5 may have been due to the variable longitudes of the TES measurements, so the actual dust opacity at the landing sites may have been less variable.

[Figure 5]

Values of τ at the landing sites of both Spirit and Opportunity were about 0.2 from 1 December to 10 December. Values of τ at both sites increased slightly over the next few days, then τ at Opportunity's landing site tripled in less than one day, reaching 0.8 on 15 December. It remained extremely high, but variable, until 25 December, when it started to decrease steadily. The rate constant for exponential decay in τ between 25 December and 8 January was about $(23 \text{ days})^{-1}$. The rate of decay of τ was three times slower than this between 8 January and 31 January. The dust optical depth after a regional dust storm can decrease due to advection of the dust to other longitudes by winds, which can be relatively fast, and fallout of the dust, which is often slower. The faster decay timescale in late December/early January likely represents clearing of the dust by horizontal winds. The decay timescale in mid/late January was longer because the dust at equatorial latitudes was well-mixed in longitude by this time, which prevented horizontal winds from removing dust from above Opportunity's landing site. Meanwhile, τ at Spirit's landing site increased from 0.2 on 1 December to 0.3 around 21 December and remained between 0.30 and 0.35 until around 25 January. Dust opacities at both landing sites were very similar before 14 December. They were also very similar after 19 January, although the dust opacities were 50% greater in late January than in early December. On the day of Spirit's EDL, τ at Spirit's landing site was 0.34 and τ at Opportunity's landing site was 0.42. On the day of Opportunity's EDL, τ at Spirit's landing site was 0.30 and τ at Opportunity's landing site was 0.28. The local and global-scale dust content of the atmosphere was greater for Spirit's

EDL than for Opportunity's, which may account for some of the differences between the two profiles, such as the differences in middle atmospheric temperatures and the differences in temperature oscillations.

6.2. Surface Pressure

The surface pressure, p_s, can be estimated and compared to other observations using:

$$p_s = p_p \exp\left((r_p - r_s)/H_p\right) \tag{7}$$

$$H_p = \frac{RT_p}{\mu g_p} \tag{8}$$

where the subscript p indicates values at parachute deployment. The estimated surface pressures are 720 ± 110 Pa for Spirit and 610 ± 110 Pa for Opportunity, which are consistent with the 1.8 km altitude difference between the two landing sites. Independent estimates of surface pressure can be obtained using Viking lander pressure data, corrected for differences in altitude between the Viking and MER landing sites, from the appropriate season. The Viking data suggest a surface pressure of 620 Pa for Spirit's landing and 630 Pa for Opportunity's landing. These values are within the above error bars. The Mars Climate Database predicts surface pressures of ∼600 Pa at both landing sites, which are also consistent with the estimated surface pressures (Forget et al., 1999).

6.3. Comparison to TES T(p) Profiles

The MGS TES instrument observed temperature as a function of pressure between the surface and 10 Pa near the two landing sites before and after the landings (Smith et al., 2001). For each MER, the entry profile and 21 TES profiles that span a period from ten

days before to ten days after the day of EDL are shown in Figures 6–7. One TES profile was selected from each day as being the closest in latitude, longitude, and LST to the EDL conditions. The vertical resolution of the TES instrument is about one scale height (Conrath et al., 2000). Uncertainties in its derived atmospheric temperatures at these altitudes are ~ 4 K (Smith, 2004).

For Spirit, the entry profile and the TES profiles both show temperatures ~ 190 K at 30 Pa and ~ 220 K at 300 Pa. For Opportunity, the entry profile and the TES profiles both show temperatures ~ 180 K at 30 Pa and ~ 220 K at 300 Pa. The TES profiles for Spirit's entry are more variable than those for Opportunity's. This could be due to the significantly larger regional topographic variations near Gusev Crater than near Meridiani Planum or to relatively rapid changes in atmospheric dust loading at the time of the Spirit landing (Golombek et al., 2003). The most striking features of the entry profiles at low altitudes are around 200 Pa, where Spirit's profile contains a near-inversion and Opportunity's profile contains a strong inversion. A similar inversion was observed in the Pathfinder entry profile (Magalhães et al., 1999; Haberle et al., 1999; Colaprete et al., 1999; Colaprete and Toon, 2000; Hinson and Wilson, 2004). Such inversions are not seen in the TES profiles, but the vertical scale of these inversions is smaller than the TES vertical resolution. However, Section 5 demonstrated that temperatures determined at these altitudes from entry profiles can be biased by tens of Kelvin due to the unknown wind velocity and poorly known angle of attack. This MER-TES comparison is the first direct comparison of atmospheric profiles derived from accelerometer data and independent observations since the PAET experiment in the terrestrial atmosphere in 1971 (Seiff et al., 1973).

[Figure 6–7]

6.4.   Comparison to Previous Entry Profiles

Figure 8 shows temperature-pressure profiles from Viking Lander 1, Viking Lander 2, Mars Pathfinder, Spirit, and Opportunity. Viking Lander 1 landed at 22°N, 312°E on 20 July 1976, when Ls was 96° and LST was 16:13. Viking Lander 2 landed at 48°N, 134°E on 3 September 1976, when Ls was 117° and LST was 09:49. Mars Pathfinder landed at 19°N, 326°E on 4 July 1997, when Ls was 143° and LST was 02:58 (Seiff and Kirk, 1977; Magalhães et al., 1999). Corresponding values for Spirit and Opportunity are shown in Table 1. All profiles, except Spirit's, contain large amplitude, long wavelength oscillations around 1 Pa. Pathfinder's temperatures are relatively cold around 0.1–1 Pa. Viking 1 temperatures are relatively cold around 10 Pa, whereas Spirit's temperatures are relatively warm around 10–100 Pa. These five profiles show how absolute temperatures, lapse rates, and temperature oscillations can vary due to changes in season, latitude, time of day, and dust content. Future analyses of these profiles may quantify which of these possible causes were responsible for the observed similarities and differences between them. This would increase our understanding of the physical processes that determine the thermal structure and dynamics of the martian atmosphere by transferring mass, momentum, and energy within the system.

[Figure 8]

7.   Conclusions

Acceleration measurements made by Spirit and Opportunity during their descents into the martian atmosphere have been used to reconstruct the entry trajectories of both spacecraft and to derive profiles of atmospheric density, pressure, and temperature along these trajectories. These are the first high-resolution measurements of the extended vertical

structure of the martian atmosphere made soon after a moderate dust storm. There are few observations of the impact of dust storms on the middle/upper regions of the martian atmosphere. The two MER temperature profiles show interesting differences in their middle atmospheric temperatures, the presence or absence of large-amplitude, long-wavelength oscillations, and their temperatures below about 20 km. Explanations of these features might require consideration of the local, regional, and global-scale dust loading in the atmosphere, the large-scale dynamics of the atmosphere, and local topography.

The Spirit and Opportunity entry profiles agree on a broad scale with TES profiles (Clancy et al., 2000; Wilson and Richardson, 2000). However, uncertainties in atmospheric winds and the angle of attack can cause errors of tens of Kelvin in these entry profiles at low altitudes. Some pieces of information that could improve the results of this paper, such as the entry states and the orientation of the gyroscope axes, have not yet been published by the MER project. As illustrated by the example in Section 5, errors of a few degrees in the angle of attack can cause the axial acceleration to differ from the acceleration parallel to the atmosphere-relative velocity vector by less than 1%. This appears small, but when decelerating from 5000 m s^{-1} to 500 m s^{-1} it corresponds to the difference between travelling at 500 m s^{-1} or 450 m s^{-1}, or 10%. It also corresponds to a 20% difference in reconstructed density. Future entry vehicles should determine their angle of attack as accurately as possible, even if aerodynamic stability is likely to keep it below 5°, so that atmospheric properties can be reconstructed accurately.

Tabulated results from this paper are available as Supplemental Information from the Icarus website. We hope to submit them to the long-term archives of the Planetary Data System. At present, these results and the software used to generate them are also available online at http://www.buimaging.com/withers/.

Acknowledgments

REFERENCES

Allison, M., McEwen, M., 2000. A post-Pathfinder evaluation of areocentric solar coordinates with improved timing recipes for Mars seasonal/diurnal climate studies. Planet. Space Sci. 48, 215–235.

Banfield, D., Conrath, B., Pearl, J. C., Smith, M. D., Christensen, P., 2000. Thermal tides and stationary waves on Mars as revealed by Mars Global Surveyor Thermal Emission Spectrometer. J. Geophys. Res. 105, 9521–9538.

Bridger, A. F. C., Murphy, J. R., 1998. Mars' surface pressure tides and their behavior during global dust storms. J. Geophys. Res. 103, 8587–8602.

Clancy, R. T., Sandor, B. J., Wolff, M. J., Christensen, P. R., Smith, M. D., Pearl, J. C., Conrath, B. J., Wilson, R. J., 2000. An intercomparison of ground-based millimeter, MGS TES, and Viking atmospheric temperature measurements: Seasonal and interannual variability of temperatures and dust loading in the global Mars atmosphere. J. Geophys. Res. 105 (E4), 9553–9572.

Colaprete, A., Toon, O. B., 2000. The radiative effects of martian water ice clouds on the local atmospheric temperature profile. Icarus 145, 524–532.

Colaprete, A., Toon, O. B., Magalhães, J. A., 1999. Cloud formation under Mars Pathfinder conditions. J. Geophys. Res. 104 (E4), 9043–9054.

Conrath, B. J., Pearl, J. C., Smith, M. D., Maguire, W. C., Christensen, P. R., Dason, S., Kaelberer, M. S., 2000. Mars Global Surveyor Thermal Emission Spectrometer (TES) observations: Atmospheric temperatures during aerobraking and science phasing. J. Geophys. Res. 105, 9509–9520.

Crisp, J. A., Adler, M., Matijevic, J. R., Squyres, S. W., Arvidson, R. E., Kass, D. M., 2003. Mars Exploration Rover mission. J. Geophys. Res. 108 (E12), 8061, 10.1029/2002JE002038.

Desai, P. N., Knocke, P. C., 2004. Mars Exploration Rover Entry, Descent, and Landing Trajectory Analysis. In: American Institute of Aeronautics and Astronautics paper 2004-5092, 42nd AIAA Aerospace Science Meeting in Reno, Nevada, USA.

Desai, P. N., Schoenenberger, M., Cheatwood, F. M., 2003. Mars Exploration Rover Six-Degree-of-Freedom Entry Trajectory Analysis. Advances in the Astronautical Sciences 116 (3), 2219–2235.

Forget, F., Hourdin, F., Fournier, R., Hourdin, C., Talagrand, O., Collins, M., Lewis, S. R., Read, P. L., Huot, J., 1999. Improved general circulation models of the Martian atmosphere from the surface to above 80 km. J. Geophys. Res. 104, 24155–24176.

Garvin, J. B., Weitz, C., Figueroa, O., Crisp, J., 2003. Introduction to the special section: Mars Exploration Rover mission and landing sites. Journal of Geophysical Research (Planets) 108 (E12), 10.1029/2003JE002072.

Golombek, M. P., Grant, J. A., Parker, T. J., Kass, D. M., Crisp, J. A., Squyres, S. W., Haldemann, A. F. C., Adler, M., Lee, W. J., Bridges, N. T., Arvidson, R. E., Carr, M. H., Kirk, R. L., Knocke, P. C., Roncoli, R. B., Weitz, C. M., Schofield, J. T., Zurek, R. W., Christensen, P. R., Fergason, R. L., Anderson, F. S., Rice, J. W., 2003. Selection of the Mars Exploration Rover landing sites. Journal of Geophysical Research (Planets) 108 (E12), 10.1029/2003JE002074.

Haberle, R. M., Joshi, M. M., Murphy, J. R., Barnes, J. R., Schofield, J. T., Wilson, G., Lopez-Valverde, M., Hollingsworth, J. L., Bridger, A. F. C., Schaeffer, J., 1999.

General circulation model simulations of the Mars Pathfinder atmospheric structure investigation/meteorology data. J. Geophys. Res. 104 (E4), 8957–8974.

Hinson, D. P., Wilson, R. J., 2004. Temperature inversions, thermal tides, and water ice clouds in the Martian tropics. J. Geophys. Res. 109, E01002, 10.1029/2003JE002129.

Kass, D. M., Schofield, J. T., Crisp, J., Bailey, E. S., Konefat, E. H., Lee, W. J., Litty, E. C., Manning, R. M., San Martin, A. M., Willis, R. J., Beebe, R. F., Murphy, J. R., Huber, L. F., 2004. PDS volume MERIMU_0001. In: MER1/MER2-M-IMU-4-EDL-V1.0, NASA Planetary Data System.

Keating, G. M., Bougher, S. W., Zurek, R. W., Tolson, R. H., Cancro, G. J., Noll, S. N., Parker, J. S., Schellenberg, T. J., Shane, R. W., Wilkerson, B. L., Murphy, J. R., Hollingsworth, J. L., Haberle, R. M., Joshi, M., Pearl, J. C., Conrath, B. J., Smith, M. D., Clancy, R. T., Blanchard, R. C., Wilmoth, R. G., Rault, D. F., Martin, T. Z., Lyons, D. T., Esposito, P. B., Johnston, M. D., Whetzel, C. W., Justus, C. G., Babicke, J. M., 1998. The Structure of the Upper Atmosphere of Mars: In Situ Accelerometer Measurements from Mars Global Surveyor. Science 279, 1672–1676.

Leovy, C. B., 2001. Weather and climate on Mars. Nature 412, 245–249.

Leovy, C. B., Zurek, R. W., 1979. Thermal tides and Martian dust storms - Direct evidence for coupling. J. Geophys. Res. 84, 2956–2968.

Lodders, K., Fegley, B., 1998. *The planetary scientist's companion*. Oxford University Press.

Magalhães, J. A., Schofield, J. T., Seiff, A., 1999. Results of the Mars Pathfinder atmospheric structure investigation. J. Geophys. Res. 104 (E4), 8943–8956.

Murphy, J. R., Toon, O. B., Haberle, R. M., Pollack, J. B., 1990. Numerical simulations of the decay of Martian global dust storms. J. Geophys. Res. 95, 14629–14648.

Pollack, J. B., Colburn, D. S., Flasar, F. M., Kahn, R., Carlston, C. E., Pidek, D. G., 1979. Properties and effects of dust particles suspended in the Martian atmosphere. J. Geophys. Res. 84, 2929–2945.

Rafkin, S. C. R., Michaels, T. I., 2003. Meteorological predictions for 2003 Mars Exploration Rover high-priority landing sites. Journal of Geophysical Research (Planets) 108 (E12), 10.1029/2002JE002027.

Schoenenberger, M., Cheatwood, F. M., Desai, P. N., 2005. Static Aerodynamics of the Mars Exploration Rover Entry Capsule. In: American Institute of Aeronautics and Astronautics paper 2005-0056, 43rd AIAA Aerospace Science Meeting in Reno, Nevada, USA.

Seiff, A., Kirk, D. B., 1977. Structure of the atmosphere of Mars in summer at mid-latitudes. J. Geophys. Res. 82, 4364–4378.

Seiff, A., Kirk, D. B., Knight, T. C. D., Young, R. E., Mihalov, J. D., Young, L. A., Milos, F. S., Schubert, G., Blanchard, R. C., Atkinson, D., 1998. Thermal structure of Jupiter's atmosphere near the edge of a 5-μm hot spot in the north equatorial belt. J. Geophys. Res. 103, 22857–22890.

Seiff, A., Kirk, D. B., Young, R. E., Blanchard, R. C., Findlay, J. T., Kelly, G. M., Sommer, S. C., 1980. Measurements of thermal structure and thermal contrasts in the atmosphere of Venus and related dynamical observations - Results from the four Pioneer Venus probes. J. Geophys. Res. 85 (A13), 7903–7933.

Seiff, A., Reese, D. E., Sommer, S. C., Kirk, D. B., Whiting, E. E., Niemann, H. B., 1973. PAET: An Entry Probe Experiment in the Earth's Atmosphere. Icarus 18, 525–563.

Smith, D., Neumann, G., Arvidson, R. E., Guinness, E. A., Slavney, S., 2003. Mars Global Surveyor Laser Altimeter Mission Experiment Gridded Data Record IEG025_A.TAB. In: MGS-M-MOLA-5-MEGDR-L3-V1.0, NASA Planetary Data System.

Smith, D. E., Lerch, F. J., Nerem, R. S., Zuber, M. T., Patel, G. B., Fricke, S. K., Lemoine, F. G., 1993. An improved gravity model for Mars: Goddard Mars Model 1. J. Geophys. Res. 98, 20871–20889.

Smith, M. D., 2004. Interannual variability in TES atmospheric observations of Mars during 1999-2003. Icarus 167, 148–165.

Smith, M. D., Pearl, J. C., Conrath, B. J., Christensen, P. R., 2001. Thermal Emission Spectrometer results: Mars atmospheric thermal structure and aerosol distribution. J. Geophys. Res. 106, 23929–23945.

Spencer, D. A., Blanchard, R. C., Braun, R. D., W., T. S., 1999. Mars Pathfinder entry, descent, and landing reconstruction. J. Spacecraft and Rockets 36 (3), 357–366.

Squyres, S. W., Arvidson, R. E., Bell, J. F., Brückner, J., Cabrol, N. A., Calvin, W., Carr, M. H., Christensen, P. R., Clark, B. C., Crumpler, L., Des Marais, D. J., d'Uston, C., Economou, T., Farmer, J., Farrand, W., Folkner, W., Golombek, M., Gorevan, S., Grant, J. A., Greeley, R., Grotzinger, J., Haskin, L., Herkenhoff, K. E., Hviid, S., Johnson, J., Klingelhöfer, G., Knoll, A., Landis, G., Lemmon, M., Li, R., Madsen, M. B., Malin, M. C., McLennan, S. M., McSween, H. Y., Ming, D. W., Moersch, J., Morris, R. V., Parker, T., Rice, J. W., Richter, L., Rieder, R., Sims, M., Smith, M., Smith, P., Soderblom, L. A., Sullivan, R., Wänke, H., Wdowiak, T., Wolff, M., Yen, A., 2004a. The Spirit Rover's Athena Science Investigation at Gusev Crater, Mars. Science 305, 794–800.

Squyres, S. W., Arvidson, R. E., Bell, J. F., Brückner, J., Cabrol, N. A., Calvin, W., Carr, M. H., Christensen, P. R., Clark, B. C., Crumpler, L., Des Marais, D. J., d'Uston, C., Economou, T., Farmer, J., Farrand, W., Folkner, W., Golombek, M., Gorevan, S., Grant, J. A., Greeley, R., Grotzinger, J., Haskin, L., Herkenhoff, K. E., Hviid, S., Johnson, J., Klingelhöfer, G., Knoll, A. H., Landis, G., Lemmon, M., Li, R., Madsen, M. B., Malin, M. C., McLennan, S. M., McSween, H. Y., Ming, D. W., Moersch, J., Morris, R. V., Parker, T., Rice, J. W., Richter, L., Rieder, R., Sims, M., Smith, M., Smith, P., Soderblom, L. A., Sullivan, R., Wänke, H., Wdowiak, T., Wolff, M., Yen, A., 2004b. The Opportunity Rover's Athena Science Investigation at Meridiani Planum, Mars. Science 306, 1698–1703.

Toigo, A. D., Richardson, M. I., 2003. Meteorology of proposed Mars Exploration Rover landing sites. Journal of Geophysical Research (Planets) 108 (E12), 10.1029/2003JE002064.

Tyler, G. L., Balmino, G., Hinson, D. P., Sjogren, W. L., Smith, D. E., Woo, R., Armstrong, J. W., Flasar, F. M., Simpson, R. A., Priest, P., 2000. PDS volume MORS_1006. In: MGS-M-RSS-5-SDP-V1.0, NASA Planetary Data System.

Tyler, G. L., Balmino, G., Hinson, D. P., Sjogren, W. L., Smith, D. E., Woo, R., Asmar, S. W., Connally, M. J., Hamilton, C. L., Simpson, R. A., 1992. Radio Science Investigations With Mars Observer. J. Geophys. Res. 97, 7759–7779.

Wilson, R. J., Richardson, M. I., 2000. The Martian Atmosphere During the Viking Mission, I: Infrared Measurements of Atmospheric Temperatures Revisited. Icarus 145, 555–579.

Withers, P., Bougher, S. W., Keating, G. M., 2003a. The effects of topographically-controlled thermal tides in the martian upper atmosphere as seen by the MGS accelerometer. Icarus 164, 14–32.

Withers, P., Towner, M. C., Hathi, B., Zarnecki, J. C., 2003b. Analysis of entry accelerometer data: A case study of Mars Pathfinder. Planet. Space Sci. 51, 541–561.

Zurek, R. W., Barnes, J. R., Haberle, R. M., Pollack, J. B., Tillman, J. E., Leovy, C. B., 1992. Dynamics of the atmosphere of Mars. In: Kieffer, H. H., Jakosky, B. M., Snyder, C. W., Matthews, M. S. (Eds.), Mars. University of Arizona Press, pp. 835–933.

Table 1: Locations and Times of MER Landings

	Spirit	Opportunity
Date[a](UTC)	4 January 2004	25 January 2004
Time of first impact[a](UTC hrs)	04:26	04:55
L_s[b](degrees)	327.7	339.1
Latitude[a],[c](°N)	-14.571892	-1.948282
Longitude[a],[c](°E)	175.47848	354.47417
Radial distance[d](km)	3392.3	3394.1
Local True Solar Time[b](hrs)	14:16	13:13

[a]Kass et al. (2004)

[b]From Mars24 Sunclock, http://www.giss.nasa.gov/tools/mars24/, based on Allison and McEwen (2000)

[c]Final landed position, not position of first impact

[d]Smith et al. (2003)

Table 2: Estimated Entry States With 1-σ Uncertainties

	Spirit	Opportunity
Time - t_{ref} (SCLK[a]seconds)	2085.625 ± 0	8194.625 ± 0
t_{ref} (SCLK seconds)	126460000.000 ± 0	128270000.000 ± 0
Radial distance (km)	3522.2 ± 1.7	3522.2 ± 1.7
Areocentric latitude (°N)	-17.7 ± 0.04	-2.9 ± 0.04
Areocentric longitude (°E)	161.8 ± 0.01	340.9 ± 0.01
Speed[b](km s^{-1})	$5.63 \pm (7 \times 10^{-4})$	$5.70 \pm (7 \times 10^{-4})$
Flight path angle[c](degrees)	11.5 ± 0.02	11.5 ± 0.02
Azimuth[d](degrees)	79.0 ± 0.02	86.5 ± 0.02

[a]SCLK = spacecraft clock

[b]Relative to a Mars-centred inertial frame (Spencer et al., 1999; Withers et al., 2003b)

[c]Angle below horizontal of velocity vector in inertial frame

[d]Angle east of north of velocity vector in inertial frame

Table 3:   Conditions at Parachute Deployment With 1-σ Uncertainties

	Spirit	Opportunity
Time - t_{ref} (SCLK seconds)	2336.375 ± 0	8444.625 ± 0
Altitude (km)	7.5 ± 1.7	6.2 ± 1.8
v_{rel} (m s^{-1})	410.98 ± 0.77	429.68 ± 0.81
Latitude (°N)	-14.528 ± 0.039	-1.957 ± 0.041
Longitude (°E)	175.411 ± 0.013	354.413 ± 0.013

Figure Captions

Figure 1: Reconstructed atmospheric structure for Spirit above parachute deployment. 1-σ uncertainties are shown on each panel by the grey envelope.

Figure 2: As Figure 1, but for Opportunity.

Figure 3: Six temperature profiles from Spirit sensitivity studies. Case A: Angle of attack = 5°. Case B: Zonal wind speed =+30 m s^{-1}. Case C: Angle of attack = 5° and zonal wind speed =+30 m s^{-1}. Case D: Zonal wind speed =-30 m s^{-1}. Case C: Angle of attack = 5° and zonal wind speed =-30 m s^{-1}. Case N: As Figure 1. The order of the cases, from low to high temperatures, is B, C, N, A, D, E.

Figure 4: As Figure 3, but for Opportunity.

Figure 5: TES infrared dust opacity during December 2003 and January 2004. Values near Spirit's landing site are shown by diamonds, values near Opportunity's landing site are shown by crosses. The times of the landings of Spirit and Opportunity are marked.

Figure 6: Comparison of entry profile and TES profiles for Spirit. The thick solid line is a 5-point running mean of Spirit's results. The thin solid lines are 21 TES profiles from a ± 10 sol window centred on the sol of EDL. The TES profile from the sol of EDL lies close to the centre of the cluster of TES profiles. Uncertainties are not shown.

Figure 7: As Figure 6, but for Opportunity.

Figure 8: Entry profiles from Viking Landers 1 and 2, Mars Pathfinder, Spirit, and Opportunity. Viking data are taken from Seiff and Kirk (1977), who tabulated their results at 4 km intervals. Viking pressure and temperature results below 28 km were not obtained using accelerometer data and are not shown here. Squares indicate Viking Lander 1, triangles indicate Viking Lander 2. Pathfinder data (unmarked solid line) are taken from

PDS volume MPAM_0001, which has a 4 Hz sampling rate (Magalhães et al., 1999). Spirit (dashed line) and Opportunity (dotted line) data come from the present paper. 5-point running means of the Pathfinder, Spirit, and Opportunity profiles are shown to reduce distracting high frequency oscillations. Uncertainties are not shown.
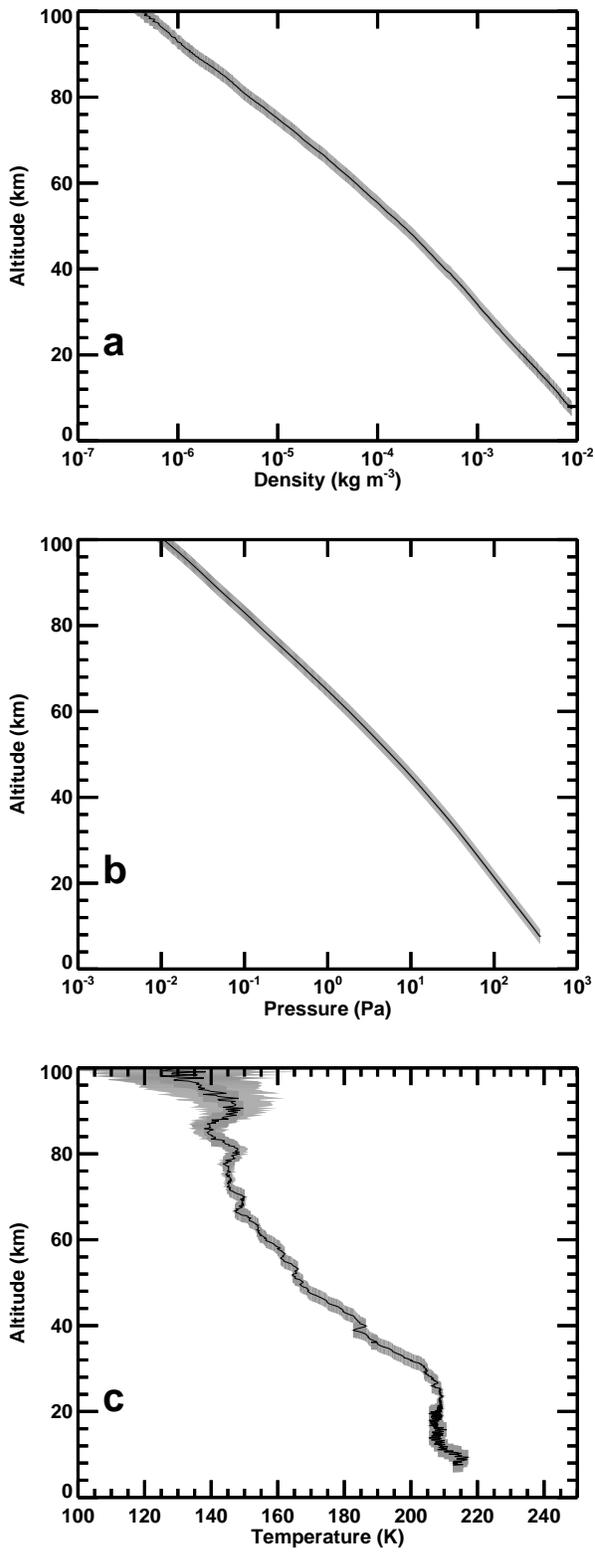
Fig. 1.— Author Paul Withers — Atmospheric Entry Profiles from Spirit and Opportunity
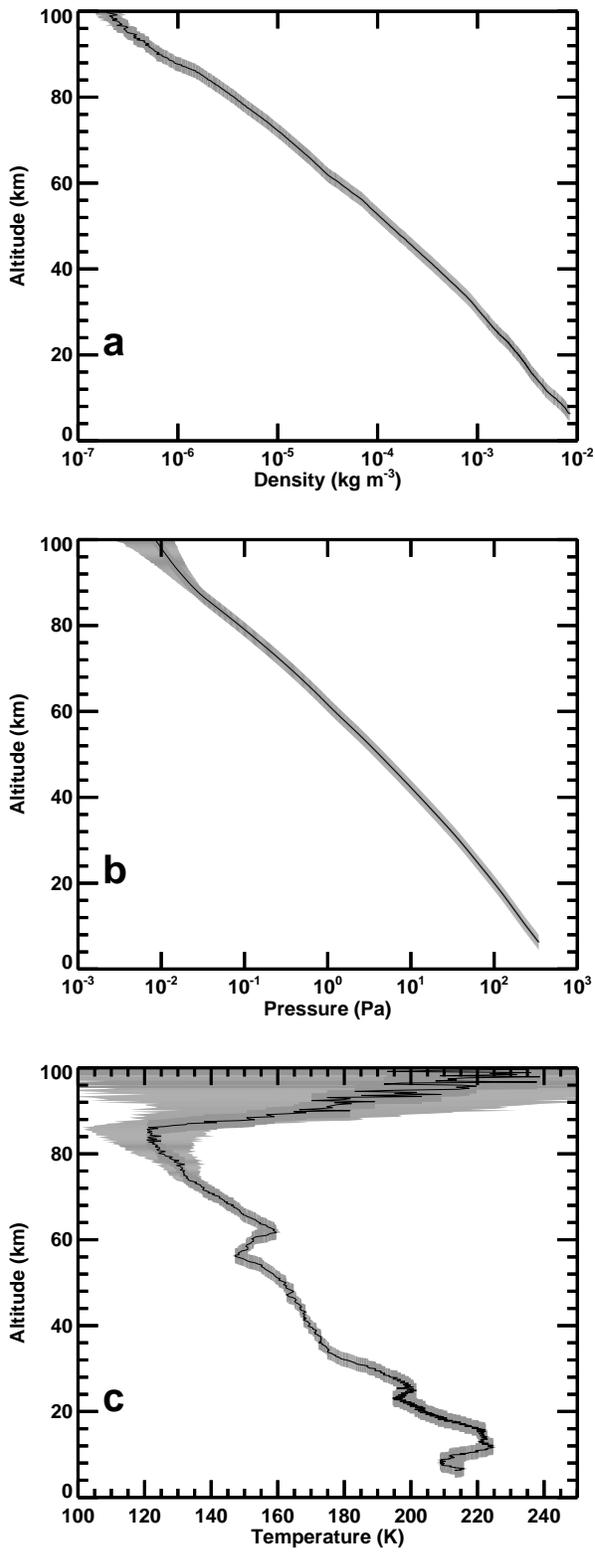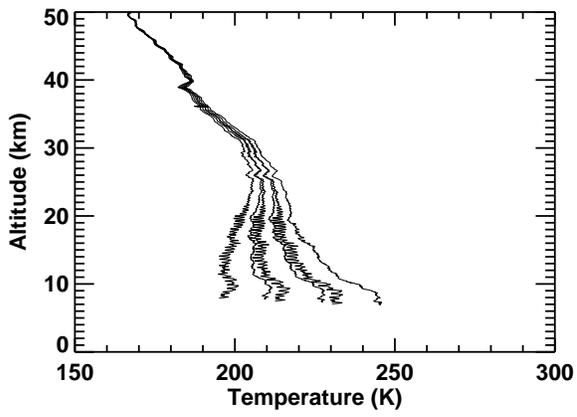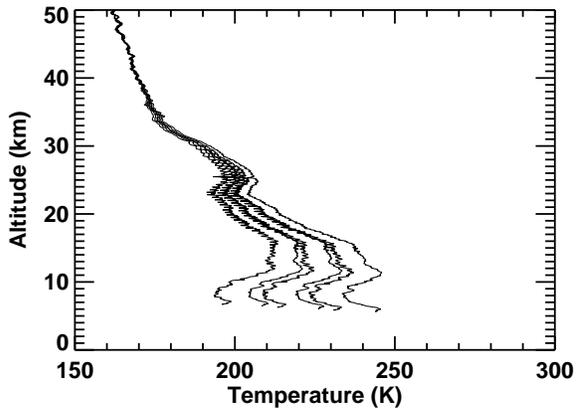
Fig. 2.— Author Paul Withers — Atmospheric Entry Profiles from Spirit and Opportunity

Fig. 3.— Author Paul Withers — Atmospheric Entry Profiles from Spirit and Opportunity

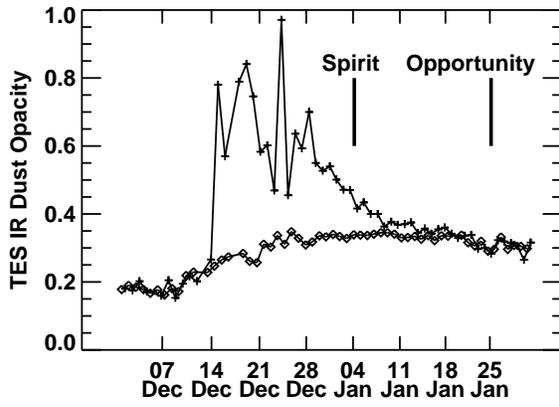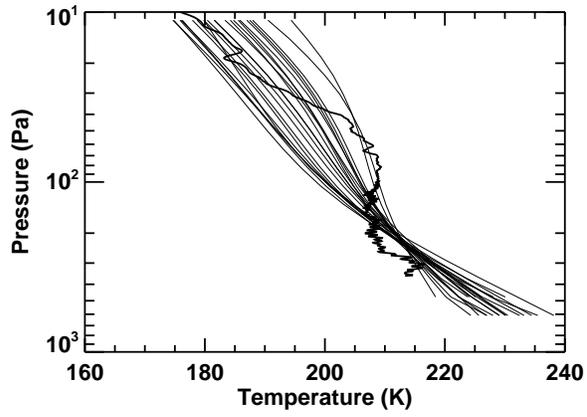Fig. 4.— Author Paul Withers — Atmospheric Entry Profiles from Spirit and Opportunity

Fig. 5.— Author Paul Withers — Atmospheric Entry Profiles from Spirit and Opportunity

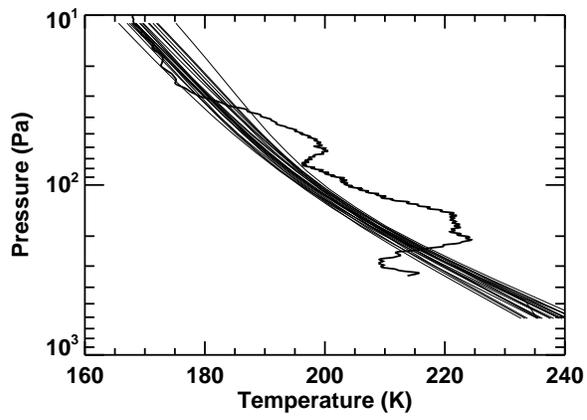Fig. 6.— Author Paul Withers — Atmospheric Entry Profiles from Spirit and Opportunity

Fig. 7.— Author Paul Withers — Atmospheric Entry Profiles from Spirit and Opportunity
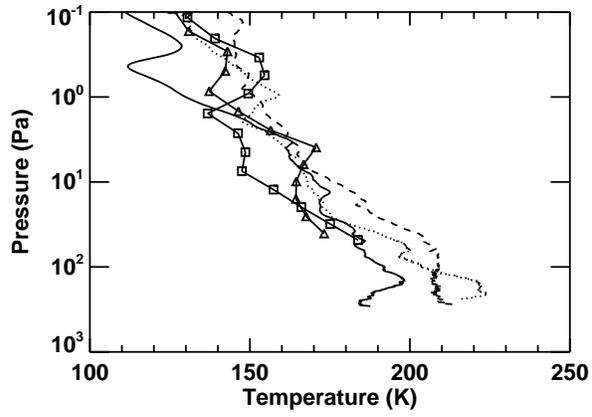
Fig. 8.— Author Paul Withers — Atmospheric Entry Profiles from Spirit and Opportunity